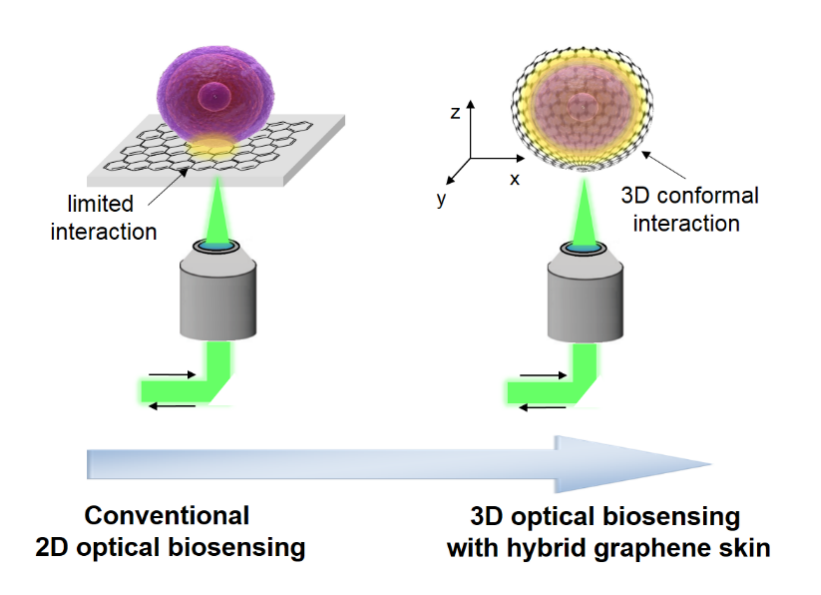
# Self-folding hybrid graphene skin for 3D biosensing

Weinan Xu,<sup>†</sup> Santosh K. Paidi,<sup>‡</sup> Zhao Qin,<sup>§</sup> Qi Huang,<sup>†</sup> Chi-Hua Yu,<sup>§</sup> Jayson V. Pagaduan,<sup>†</sup> Markus J. Buehler,<sup>§</sup> Ishan Barman,<sup>‡,∥,⊥</sup> David H. Gracias\*,<sup>†,</sup>,<sup>∇</sup>

- <sup>†</sup>Department of Chemical and Biomolecular Engineering, Johns Hopkins University, Baltimore, Maryland 21218, USA
- <sup>‡</sup> Department of Mechanical Engineering, Johns Hopkins University, Baltimore, Maryland 21218, USA
- § Department of Civil and Environmental Engineering, Massachusetts Institute of Technology, Cambridge, Massachusetts 02139, USA.
- Department of Oncology, The Johns Hopkins University School of Medicine, Baltimore, Maryland, 21287, USA
- $^{\perp}$  The Russell H. Morgan Department of Radiology and Radiological Science, The Johns Hopkins University School of Medicine, Baltimore, Maryland 21287, USA
- $^{\triangledown}$  Department of Materials Science and Engineering, Johns Hopkins University, Baltimore, Maryland 21218, USA

# **TOC Figure**



**ABSTRACT** 

Biological samples such as cells have complex three-dimensional (3D) spatio-molecular profiles

and often feature soft and irregular surfaces. Conventional biosensors are based largely on 2D and

rigid substrates, which have limited contact area with the entirety of the surface of biological

samples making it challenging to obtain 3D spatially resolved spectroscopic information,

especially in a label-free manner. Here, we report an ultrathin, flexible skin-like biosensing

platform that is capable of conformally wrapping a soft or irregularly shaped 3D biological sample

such as a cancer cell or a pollen grain, and therefore enables 3D label-free spatially resolved

molecular spectroscopy via surface-enhanced Raman spectroscopy (SERS). Our platform features

an ultrathin thermally responsive poly(N-isopropylacrylamide)-graphene-nanoparticle hybrid skin

that can be triggered to self-fold and wrap around 3D micro-objects in a conformal manner due to

its superior flexibility. We highlight the utility of this 3D biosensing platform by spatially mapping

the 3D molecular signatures of a variety of microparticles including silica microspheres, spiky

pollen grains, and human breast cancer cells.

**KEYWORDS:** SERS, graphene, lab-on-a-chip, stimuli-responsive, origami

2

Motivated by societal needs for diagnosing diseases more efficiently, monitoring biotechnological processes, detecting biochemical warfare agents, and improving food safety, significant efforts in nanotechnology are focused on biosensing. 1,2,3 Single cell biosensors can provide detailed information on the composition and activity of individual cells as well as elucidate cellular heterogeneity and statistical variation in multicellular entities such as tissues and tumors. 4,5,6 Among the variety of biosensing techniques in development, surface-enhanced Raman spectroscopy (SERS) has unique advantages for label-free, highly sensitive and selective detection of analytes through the amplification of localized electromagnetic fields on the surface of plasmonic nanomaterials when excited with monochromatic light. 7,8 SERS measurements are non-destructive and minimally to entirely non-invasive which are advantageous for both *in-vitro* and *in-vivo* measurements. 9,10

SERS substrates are developed primarily by depositing or fabricating noble metal nanostructures<sup>11</sup> on rigid and static substrates such as glass and silicon.<sup>12</sup> While these approaches have enabled a range of biochemical studies, there are obvious limitations in the analysis of soft, irregularly shaped and three-dimensional (3D) objects that are ubiquitous in biology. To address these limitations, researchers, including ourselves, have explored the creation of flexible SERS substrates such as plasmene nanosheets, <sup>13</sup> metal nanoparticles impregnated paper, polymer membranes and electrospun fibers.<sup>14,15</sup> These flexible substrates enable better contact with 3D samples and efficient access to the analytes. However, they generally rely on relatively thick substrates, which are unable to form intimate and conformal contact with small, irregularly shaped samples such as a single cell.<sup>16</sup>

Previously, we reported a technique entitled Mechanical Trap Surface-Enhanced Raman Spectroscopy (MTSERS) wherein a self-folding microgripper<sup>17</sup> with arms composed of a bilayer

of SiO/SiO<sub>2</sub> (10/15 nm) was coated with gold nanostars.<sup>18</sup> We utilized MTSERS to encapsulate and analyze the structure of microparticles such as Janus beads and live cells.<sup>19</sup> Despite the improved access to the 3D surface, a limitation of this approach is that the arms are composed of rigid materials that preclude conformal contact to irregularly shaped objects. Besides, the folding force due to release of residual stress of the hinges, and the rigid arms of the grippers can potentially deform the encapsulated cell possibly disturbing its native biomolecular state.<sup>20</sup>

Graphene has an atomically thin two-dimensional (2D) monolayer structure with good chemical inertness and biocompatibility. Consequently, it is an attractive substrate for biosensing devices. In SERS based biosensing applications, graphene provides an atomically flat surface, high stability and a clean vibrational Raman spectrum. However, graphene shows limited intrinsic Raman enhancement, stemming solely from the charge transfer between the graphene and the analyte. Hence, graphene is often used in combination with plasmonic metal nanostructures for SERS applications. Monolayer graphene also has a Föppl–von Kármán number, which is the ratio of the in-plane to out of plane stiffness, comparable to that of paper and consequently is an ideal substrate for conformally contacting a 3D object. However, graphene with a rigid underlying substrate, which does not utilize the excellent flexibility of this 2D material.

Here, we leverage the ultrathin, low bending rigidity, biocompatibility and high stability of graphene to create a flexible, skin-like SERS substrate. The SERS skin is composed of thermally responsive graphene, which has poly(N-isopropylacrylamide) (PNIPAM) brushes grafted on the surface, and plasmonic silver nanocubes (Ag NCs). After patterning the ultrathin SERS skin into well-defined shapes, self-folding is induced by a mild temperature increase, compatible with live cell culture. Importantly, as we show, the ultrathin self-folding SERS skin conformally wraps

micro-objects with a wide range of mechanical properties and surface irregularities such as rigid microspheres, spiky pollen grains, and soft biological cells. Due to this conformal 3D SERS enhancement, we demonstrate that high fidelity molecular maps can be obtained using confocal Raman microscopy. This conformal 3D spectroscopic approach based on ultrathin skin-like structures offers an unprecedented opportunity for molecular mapping of the 3D surfaces and, in particular, represents a novel route to bridge the chemical and morphologic domains at the single cell level.

The conceptual scheme and fabrication process flow are illustrated in Figure 1. The approach relies on the conformal wrapping of a 3D object with an ultrathin flexible skin-like SERS substrate with extremely low bending rigidity. The skin-like substrate is capable of conformally coating even a spiky particle such as a pollen grain whose irregular 3D surface can then be mapped using SERS. This 3D skin should be contrasted with a conventional planar rigid SERS substrate whose short-range electromagnetic enhancement allows spectroscopic information to be measured only from analytes in the relatively small contact region between the base of the 3D object and the 2D SERS substrate (Figure 1a). In the absence of the skin, it is very challenging to achieve high-density coverage and uniform distribution of plasmonic metal nanostructures required to obtain a 3D spectroscopic SERS map. Also, without the skin, it is virtually impossible to conformally coat the surface of live cells with plasmonic nanoparticles while keeping it viable and preventing internalization. With the hybrid skin, as we show, a high density and uniform coverage of Ag NCs can be obtained and importantly our approach is also compatible with live cell culture.

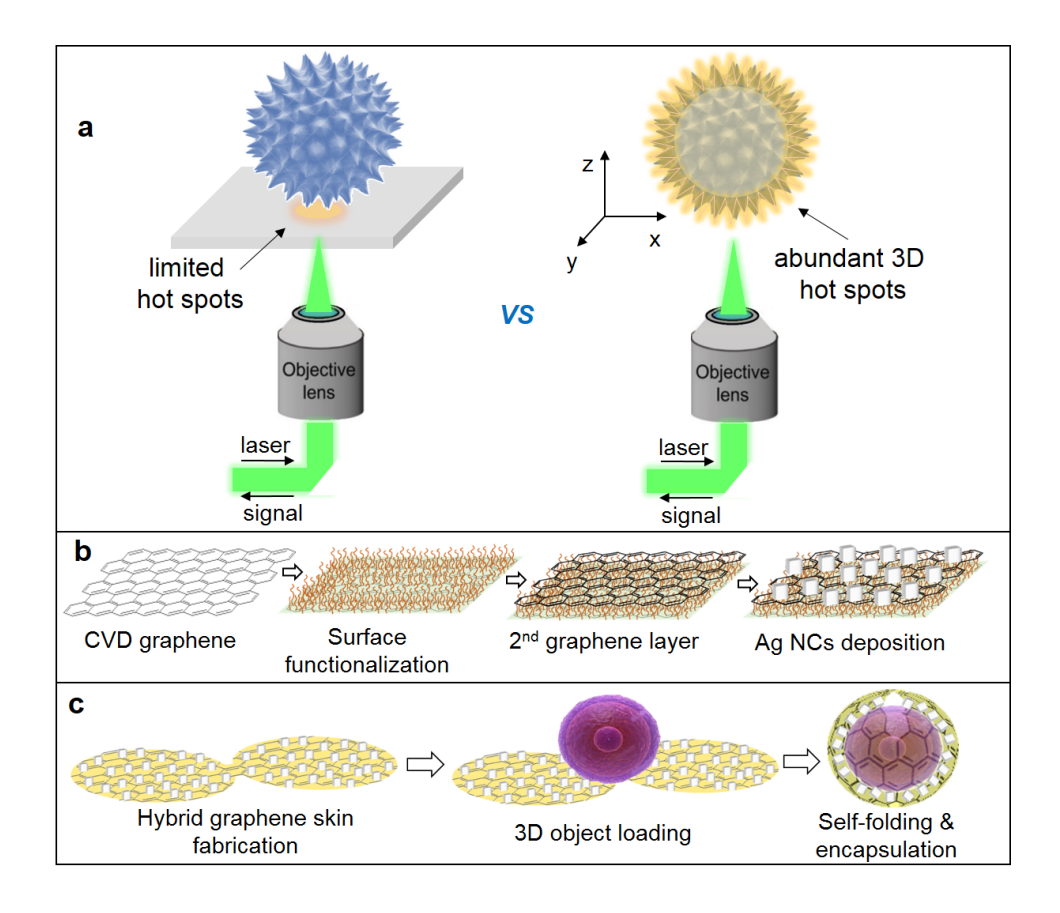


**Figure 1**. Schematic illustrations of the self-folding hybrid graphene skin for 3D biosensing. (a) Conceptual comparison of SERS analysis of a 3D irregularly shaped microobject using a conventional, rigid 2D SERS substrate (left) and the hybrid graphene skin (right). The self-folding skin can conformally wrap 3D object facilitating 3D spatially resolved SERS measurements. (b) Schematics illustrating the fabrication process of the hybrid G-PNIPAM-G-Ag film with thermal responsive properties. The surface functionalization (left to right) involves chemical grafting of PNIPAM brushes followed by transfer of a second layer of graphene and deposition of Ag NCs for SERS enhancement. (c) Schematics illustrating that the skin-like G-PNIPAM-G-Ag film can be photolithographically patterned into well-defined 2D shapes, such as a dumbbell, and then induced to self-fold into a closed 3D geometry and encapsulate 3D micro-objects by a mild increase in temperature.

In our fabrication process, as illustrated in Figure 1b, we first transferred chemical vapor deposited (CVD) monolayer graphene onto a silicon wafer from the copper foil on which it was grown. We then non-covalently surface functionalized the graphene with an ultrathin polydopamine (PD) intermediate layer, and subsequently grafted thermally responsive PNIPAM brushes; the entire details of which can be found in a previous publication.<sup>32</sup> This surface functionalization results in an ultrathin G-PNIPAM hybrid film of approximately 8-10 nm in

thickness, so that it retains a low bending stiffness to facilitate its temperature-induced bending. The thickness of the PNIPAM and PD layer can also be tuned to alter the mechanical and self-folding characteristics of the skin. To enable a pristine, direct contact and strong interactions between graphene and the Ag NCs, we transferred a second layer of CVD graphene atop of the functionalized graphene which separates the Ag NCs from the underlying PNIPAM brushes and provides a cleaner signal (Figure S1). We synthesized plasmonic Ag NCs using a polyol method,<sup>33</sup> screened ligands to obtain uniform coatings of Ag NCs, and discovered that cysteamine capped Ag NCs have a strong affinity to the graphene surface. The final G-PNIPAM-G-Ag SERS skin was formed by depositing a high density of cysteamine capped Ag NCs, with an average size of 20 nm, onto the top graphene surface.

We characterized the optical properties of the G-PNIPAM-G-Ag skin and its precursor films using UV-Vis spectroscopy (Figure 2a). The pristine CVD graphene is highly transparent with transmittance above 85% across a wide range of wavelengths ranging from 250 nm to 800 nm. After surface functionalization with temperature responsive PNIPAM brushes, the film remains highly transparent but with slightly reduced transmittance. After coating with a high density of Ag NCs, there are prominent absorbance features at 400 and 600 nm, which correspond with the localized surface plasmon resonance peaks of Ag NCs and their assembly.<sup>33</sup>

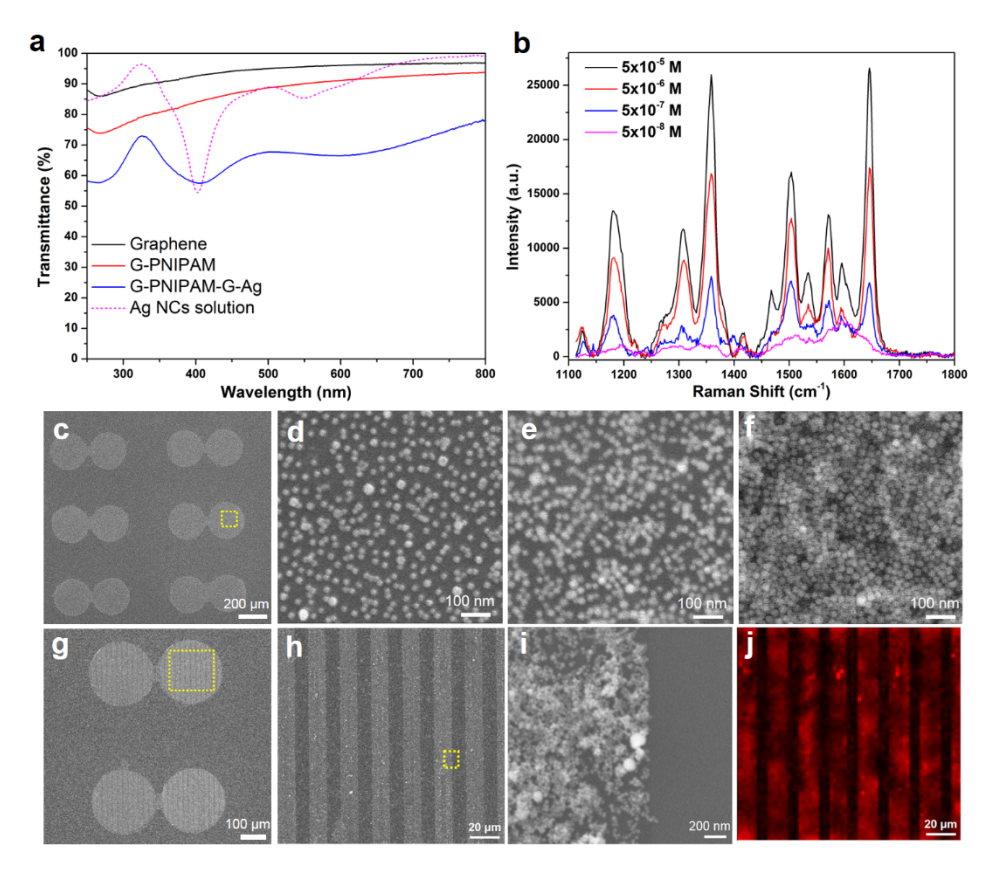


**Figure 2**. Characterization of the G-PNIPAM-G-Ag skin. (a) UV-Vis spectra of the pristine graphene, G-PNIPAM, G-PNIPAM-G-Ag film, and an aqueous solution of Ag NCs. (b) Raman spectra of different concentrations of R6G deposited on the surface of the patterned G-PNIPAM-G-Ag skin. (c-f) SEM images of the dumbbell shaped G-PNIPAM-G-Ag skin (c), with tunable Ag NCs density on its surface, as shown in the higher magnification SEM images of a representative area (dotted yellow square) with approximately (d) 750, (e) 1000, and (f) 1800 Ag NCs per μm². (g-i) SEM images of the dumbbell shaped G-PNIPAM-G-Ag skin with photolithographically defined line patterns of Ag NCs on the surface. Panels h and i are progressively zoomed in regions corresponding to the dotted yellow squares in panel g and h, respectively. (j) Raman spatial mapping of the G-PNIPAM-G-Ag skin with patterned Ag NCs lines using the R6G peak at 1310 cm⁻¹. Panel j corresponds to the same spatial region as h.

We investigated the performance of the photopatterned G-PNIPAM-G-Ag thin film as a SERS substrate by measuring spectra of a Raman reporter molecule Rhodamine 6G (R6G) deposited on the substrate (Figure 2b). We observed a strong enhancement of the major peaks of R6G, including the ones at 1180, 1310, 1359, 1504, 1571 and 1646 cm<sup>-1</sup> which can be assigned to the aromatic ring stretching modes,<sup>22</sup> with detection limit down to the nanomolar range. We estimated the Raman enhancement factor (EF) of the hybrid graphene SERS skin for R6G

molecule to be on the order of 10<sup>8</sup> (Figure S2), which is comparable with other Ag nanoparticle-based SERS substrates reported in the literature<sup>34</sup>. It is noteworthy, that bare graphene also shows a weak SERS enhancement, but it is negligible compared to the G-PNIPAM-G-Ag skin (Figure S3). Also, the Raman spectral peaks from PD and PNIPAM, which were used to functionalize the bottom graphene layer have negligible intensity as compared to those of analyte molecules such as R6G (Figure S4) and do not interfere with the SERS mapping.

An additional attractive feature is that we can tune both the density and the spatial distribution of the plasmonic nanoparticles on the G-PNIPAM-G-Ag SERS skin. We found that the density of the NCs on the patterned G-PNIPAM-G-Ag SERS skin can be varied from very low to very high density (up to 1800 particles per  $\mu$ m<sup>2</sup>; Figure 2d-f) by increasing the concentration of Ag NCs solution during its deposition on the graphene skin. A higher density of Ag NCs results in greater SERS enhancement, but as discussed later, also increases the bending rigidity of the film which is not desirable for self-folding;<sup>35</sup> therefore, we chose to use densities of about 1000 particles per  $\mu$ m<sup>2</sup> in our 3D SERS studies.

We were also able to create well-defined spatial patterns of Ag NCs on the SERS skin using photolithography prior to the deposition of Ag NCs. Figure 2g-i shows patterns of uniform Ag NCs lines with 12 µm width and 8 µm spacing on the dumbbell shaped G-PNIPAM-G-Ag skin. When we exposed these patterned substrates to the Raman reporter molecule R6G, only the linear regions patterned with the Ag NCs showed strong Raman signal due to the localized electromagnetic enhancement (Figure 2j). The ability to spatially pattern and control the distribution of nanoparticles on the SERS skin with high precision is important for its integration with other microelectronics and microfluidic devices.

The inclusion of the PNIPAM brushes endows the G-PNIPAM-G-Ag SERS skin with a unique temperature responsive self-folding capability. The self-folding process of the dumbbell shaped G-PNIPAM-G-Ag film is shown in Figure 3a, in which the two petals fold towards the center when heated in water to 37°C. The self-folding mechanism is that upon increasing the temperature above the lower critical solution temperature (LCST) of PNIPAM (approximately 33°C), the densely grafted brush layer undergoes a significant shrinkage in volume (approximately 50%), while the graphene and PD layer does not shrink.<sup>32</sup> The internal strain mismatch induces the folding of the overall structure. The bending stiffness of the G-PNIPAM-G-Ag skin increases with increasing Ag NCs density on the surface as confirmed by theoretical estimation and nanoindentation experiments (see section 3 in SI). The self-folding G-PNIPAM-G-Ag skin can also be patterned to self-fold into other 3D shapes such as a box or flower. Additionally, the Ag NCs can be replaced with other plasmonic nanostructures such as spherical gold nanoparticles (Figure S6 and S7). These results highlight the versatility of the G-PNIPAM-G-Ag skin.

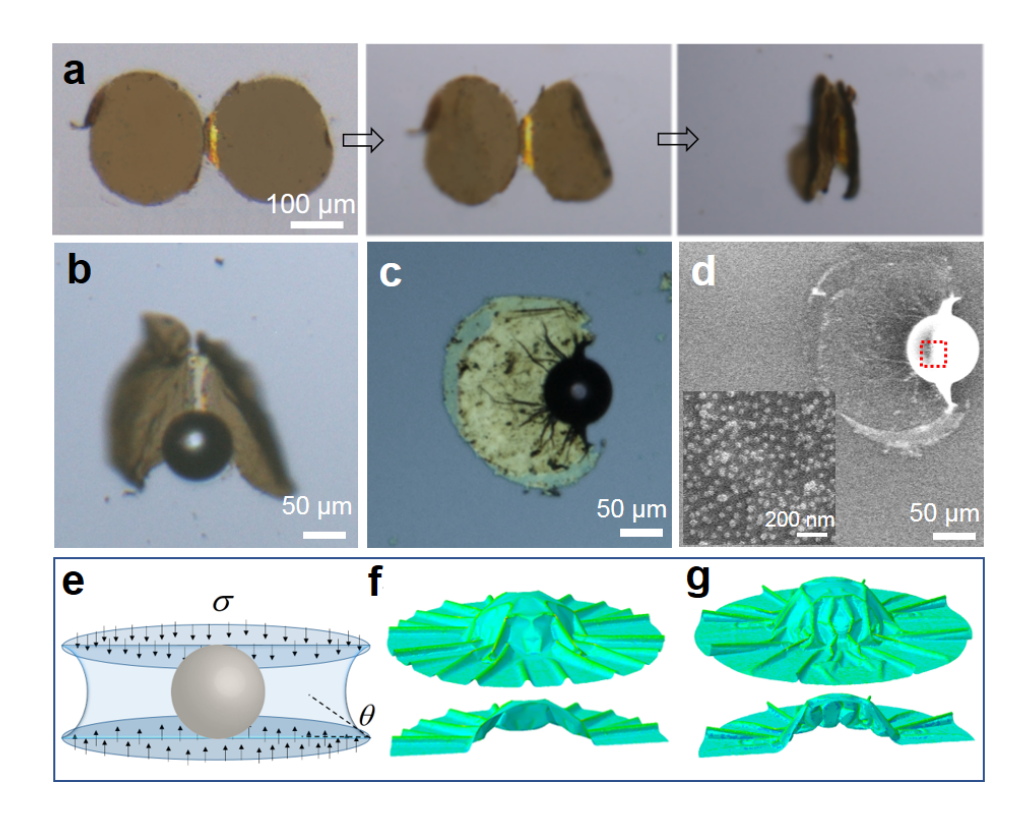


**Figure 3.** Self-folding and wrapping of a microparticle with the G-PNIPAM-G-Ag skin. (a) Optical microscopy image of the dumbbell shaped G-PNIPAM-G-Ag skin in the flat state (left panel), during (center panel), and after (right panel) thermally triggered self-folding. (b) Optical image showing the wrapping of a spherical silica microparticle using a dumbbell shaped G-PNIPAM-G-Ag skin. (c) Optical, and, (d) SEM image showing that the G-PNIPAM-G-Ag conformally wraps around the microparticle after drying with characteristic skin-like wrinkles. The inset shows a higher magnification image of the region indicated by the red dotted square and indicates that the surface of the microparticle has a high density of Ag NCs. (e) Schematic of a model illustrating the effect of the surface tension between the hybrid graphene skin and the particle during drying.  $\sigma$  and  $\theta$  indicate the Laplace pressure and contact angle. (f, g) FEM results showing the deformed graphene skin on the silica microparticle after water evaporation, with two different conditions: (f)  $\sigma$  = 219.8 Pa for  $\theta$  = 79°, and (g)  $\sigma$  = 882.8 Pa for  $\theta$  = 40°. The images show both the top view and section view of the shell model for the skin, colored by principle in-plane strain within the neutral layer ( $\varepsilon$  = 0 cyan,  $\varepsilon$  = 0.02 green).

The temperature-induced shape changes, and conformal encapsulation capability of the G-PNIPAM-G-Ag skin makes it an ideal 3D biosensing platform. As a proof of concept, the dumbbell-shaped G-PNIPAM-G-Ag skin was used to encapsulate various 3D microparticles. Figure 3b-d show the encapsulation of a silica microparticle with a diameter of 75  $\mu$ m, it is evident that after evaporation of water, the G-PNIPAM-G-Ag thin film conformally wraps the

microparticle surface due to its ultrathin structure and strong capillary forces during drying.<sup>36,37,38</sup> High resolution SEM images (Figure 3d) of the encapsulated silica microparticle show a high density of Ag NCs on the surface, which is critical for SERS enhancement.

For 3D objects analyzed after drying, the surface tension effects during water evaporation play a major role in the conformal wrapping of the hybrid graphene skin. We developed a finite element model (FEM) using the Abaqus/Explicit solver to theoretically estimate the deformation of the hybrid graphene skin during the drying process (see section 5 in the SI). If we assume that the water evaporation is a slow and quasi-static process, the system has the force balance condition (Figure 3e) as:  $\pi R^2 \sigma = -2\pi R \gamma \cos \theta$ , where  $R = 125 \,\mu\text{m}$  is the radius of the hybrid graphene skin,  $\sigma$  is the Laplace pressure from surface tension,  $\gamma = 72$  mN/m is the surface tension of water and  $\theta$  is the contact angle between water and silver nanoparticles, estimated to be in the range of  $40^{\circ}$  and  $79^{\circ}$ . Some symmetric order of the conditions, we estimate the Laplace pressure  $\sigma$  to be in the range of 219.8 Pa and 882.5 Pa. Using the mean density, bending stiffness, thickness of the skin, and loading conditions, we can effectively simulate the deformation process of the hybrid graphene skin on the microparticle, by using a shell model for the skin with the same thickness and bending stiffness and a rigid sphere for the microparticle (Figure 3f-g). We find that the Laplace pressure is large enough to drive the significant deformation of the skin and fully wrap up the microparticle. The deformation forms wrinkles in the radial direction outside the sphere, agreeing with experimental results in Fig. 3c. The wrinkles provide another mechanism to release the in-plane deformation and follow the non-zero Gaussian curvature of the sphere surface. 40 After wrapping, the van der Waals interaction between the skin and the microparticle will stabilize the closed structure.

The ultrathin skin-like nature of the G-PNIPAM-G-Ag skin allows it to conformally wrap not only regular shaped objects such as the silica microparticle discussed earlier, but also irregularly shaped 3D objects. Figure 4a-b shows the structure of an oxeye daisy pollen, which has an irregular and spiky geometry, with an average size of 35 µm. It is very challenging for conventional rigid biosensing structures and devices to form intimate contact with such spiky microparticles. From the Figure 4c-d, we observe that the G-PNIPAM-G-Ag skin conformally wraps the surface of the pollen including its spikes, and characteristic wrinkles of skin-like materials are formed along the edge or bottom of the spikes. We estimate the maximum strain on the hybrid graphene skin when wrapping the pollen spike to be approximately 2.6 % (see section 6 in SI), which is much lower that the fracture strain of graphene, which is 0.14 at room temperature.<sup>41</sup> This agrees with our observation that no fracture or tearing of the G-PNIPAM-G-Ag skin was seen on wrapping the pollen spikes.

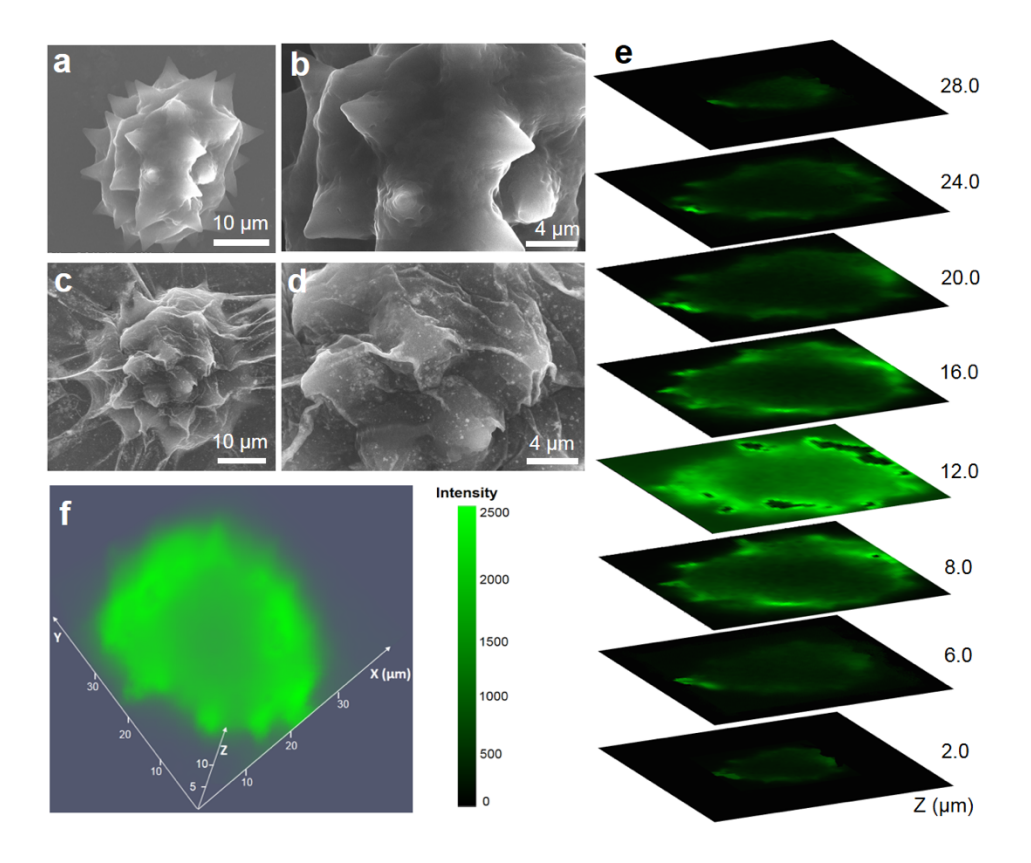


**Figure 4.** 3D SERS spatial mapping of a spiky pollen wrapped with the G-PNIPAM-G-Ag skin. (a-b) SEM image of a pristine pollen grain at different magnification. (c-d) SEM image of a pollen grain wrapped inside the G-PNIPAM-G-Ag skin, which shows characteristic skin-like wrinkles and high-density nanoparticles on the surface. (e) 2D SERS mapping of the pollen at a series of focal planes along the Z axis. (f) Reconstructed 3D surface Raman spectroscopic spatial map of the pollen showing characteristic spiky features.

High resolution SEM images show a high density of Ag NCs coating the 3D surface of the pollen grain due to conformal coating of the skin. The intimate contact between the Ag NCs with the 3D object surface allows high resolution 3D surface chemical mapping. To demonstrate this feature, the surface of the pollen was adsorbed with R6G molecules prior to its encapsulation with the G-PNIPAM-G-Ag skin. We then used the strong Raman signals of the R6G molecule on the surface of the pollen for spatial mapping using confocal Raman microscopy.

Figure 4e shows the Raman spatial mapping using the 1310 cm<sup>-1</sup> R6G peak of the spiky pollen particle at different planes along the z-axis. We observed the spiky features on the pollen

particle in the z-plane Raman maps with significantly stronger intensity along the peripheral region as compared to the internal area. Also, we were able to reconstruct the irregular 3D surface of the pollen particle by integration of all the 2D Raman maps at a series of focal planes along the z-axis (Figure 4f). Such 3D non-perturbative chemical mapping cannot be easily achieved by currently available methods.

Cells, tissues and other biological samples are soft and, as a result, existing rigid SERS substrates are mechanically mismatched (leading to undesirable perturbation of the biospecimen) and do not afford ideal biosensing interfaces. Our flexible self-folding G-PNIPAM-G-Ag SERS skin can be applied for multiplexed 3D spatial mapping of these biological samples at the single cell level. We demonstrate 3D SERS mapping of cells, by encapsulating MDA-MB-231 breast cancer cells with the dumbbell shaped G-PNIPAM-G-Ag skin. We observed that the cells adhere well on G-PNIPAM-G-Ag (Figure 5a-b) and the cell culture temperature (37 °C) was sufficient to induce the folding of temperature responsive G-PNIPAM-G-Ag skin. The breast cancer cells were successfully wrapped within the skin following the temperature induced folding, and were viable up to 48 hours after encapsulation (Figure S10). The optical microscope and immunofluorescence images of the cell wrapped inside the G-PNIPAM-G-Ag skin are shown in Figure 5c-f, where the green fluorescent antibody (Alexa Fluor 488) and blue fluorescent DAPI stain were used against fibronectin and DNA, respectively. The images indicate that the morphology of wrapped cells and free cells are similar, highlighting low perturbation during the wrapping process.

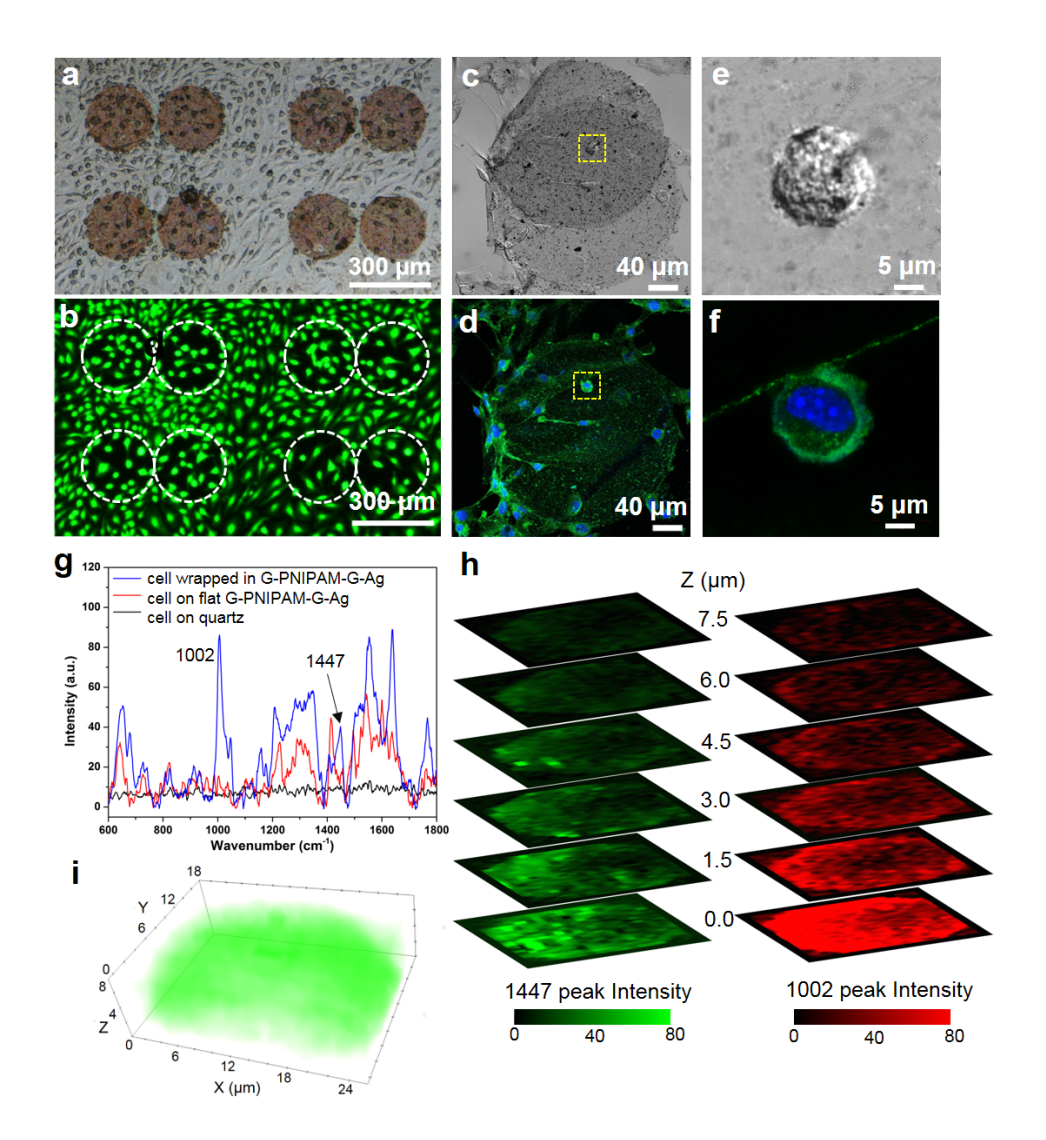


**Figure 5.** Wrapping of live breast cancer cells inside the G-PNIPAM-G-Ag skin and 3D SERS spatial mapping. (a) Bright-field, and (b) fluorescent live/dead assay (calcein AM and ethidium homodimer-1) images of the cells cultured on the surface of the 2D patterned G-PNIPAM-G-Ag skin. The dotted white circles in panel d correspond to the positions of the patterned G-PNIPAM-G-Ag dumbbells. (c) Bright field and (d) the corresponding immunofluorescence image (green: Alexa Fluor 488, blue: DAPI) of the cancer cells wrapped by the folded G-PNIPAM-G-Ag skin. The higher magnification images of a single cell in the dotted yellow square regions of panel c and d are shown in (f) and (g), respectively. (h) Raman spatial maps of the wrapped cell at different focal planes along the z-axis. The green color corresponds to the lipid peak intensity at 1447 cm<sup>-1</sup> and red color indicates the protein peak intensity at 1002 cm<sup>-1</sup>. (i) The reconstructed 3D Raman spatial map of the lipid peak at 1447 cm<sup>-1</sup> for a single cell wrapped by the G-PNIPAM-G-Ag skin.

We performed Raman measurements on the breast cancer cell wrapped inside the hybrid graphene skin, and detected strong signals from the lipids and relevant proteins on the cell

membrane (Figure 5g). We can attribute the spectral features as follows: 1002 cm<sup>-1</sup> (phenylalanine), 1155 cm<sup>-1</sup> (carotenoids), 1209 cm<sup>-1</sup> (stretching mode in phenylalanine), 1340 cm<sup>-1</sup> (CH<sub>2</sub> twist and bend in proteins and lipids), 1447 cm<sup>-1</sup> (C-H deformation of lipids), and 1654 cm<sup>-1</sup> (amide I). 42,43 In contrast, the MDA-MB-231 cells on the bare quartz substrate do not show any observable Raman peak under the same experimental conditions. Moreover, when the cell was on a flat G-PNIPAM-G-Ag film, there was only limited enhancement in the Raman compared with the ones wrapped inside the hybrid skin (Figure 5g). We estimate the Raman enhancement factor of the hybrid graphene SERS skin to the protein peak (1002 cm<sup>-1</sup>) and lipid peak (1447 cm<sup>-1</sup>) to be 110 and 60, respectively, which is comparable with prior SERS studies of the cell membrane. 44

The strong Raman signals form the cell membrane also facilitated 3D surface chemical mapping of the cell. For spatial mapping, we used the two major peaks: the 1002 cm<sup>-1</sup> protein peak and the 1447 cm<sup>-1</sup> lipid peak. As shown in Figure 5h, the Raman mapping of the cell at different focal planes along the z-axis using the protein and lipids peaks allowed us to study the spatial distribution of the biological components, and generate a series of 2D confocal chemical maps of the cell surface. We observed that the overall Raman intensity is strongest at the bottom z-plane corresponding to the contact region between the bottom of the cell and the G-PNIPAM-G-Ag skin. We attribute this observation to the fact that a soft biological cell tends to spread out on the substrate (Figure S10), with the largest contact area between the cell membrane and graphene SERS skin at the bottom. Of note, the geometric profile of the cell wrapped inside G-PNIPAM-G-Ag skin was not distorted, unlike the gripping force-induced cellular deformation observed in our previously reported MTSERS platform.<sup>19</sup>

Furthermore, we can use the 2D planar image stack to reconstruct a 3D chemical map of the biological cell (Figure 5i), which indicates the spatial distribution of spectral markers over the cell volume. In contrast, for the un-wrapped cancer cell (Figure S11), it is possible to achieve spatial mapping with measurable intensity only at the bottom plane which is in contact with the SERS skin. As the focal plane moves away from the bottom plane, the Raman intensity drops off sharply and there is almost no distinguishable Raman mapping. This result highlights the limited contact area of the cell with 2D planar sensors and the inability to get 3D spatial maps using 2D SERS substrates.

In conclusion, we have developed an ultrathin 3D self-folding flexible skin-like SERS substrate and demonstrated its utility in mapping the surface chemistry of both regular and irregularly shaped soft and rigid biological samples. This platform successfully tackles several challenges that have impeded the ability to capture and perform *in situ* label-free chemical analysis of single live cells in 3D. First, the ultrathin and compliant skin allows conformal and intimate contact all over the 3D object while minimizing sample perturbation and significantly improving the information that can be obtained during biosensing. Second, the self-folding and wrapping is triggered by biologically compatible conditions and does not necessitate the use of tethers or wires; hence it allows facile integration with existing microfluidic systems. Third, the skin is highly versatile and can be patterned into different shapes and sizes to encapsulate and analyze a range of objects. Fourth, the surface of the skin can also be equipped with other nanostructures or functional elements and devices, which can further expand its application to other electrical or electrochemical biosensing modalities. <sup>45</sup> Finally, the ability to rapidly and selectively profile the surfaces of cells in 3D, in conjunction with chemometric tools, would permit the study of fundamental biological processes such as cell surface glycosylation. Such analyses are challenging to perform with existing techniques due to limitations in resolution, sensitivity, and/or required experimental conditions. Consequently, we anticipate that this novel skin-encapsulation and

spectroscopic platform will be utilized to probe 3D spatio-temporal activity with single cell resolution of broad relevance to cell biology, drug discovery, and biomedical engineering.

ASSOCIATED CONTENT

**Supporting Information** 

The Supporting Information (SI) is available free of charge on the website at DOI:

The SI includes details of the experimental methods and notes on the Raman and mechanical

characteristics of the G-NIPAM-G-Ag skin, versatility of the skin, estimation of the Laplace

pressure on water evaporation, estimation of the strain during wrapping on the pollen spike and

Raman spatial mapping of a cancer cell on the skin prior to wrapping.

**AUTHOR INFORMATION** 

Corresponding Author

\*E-mail: <u>dgracias@jhu.edu</u>.

**Notes** 

The authors declare no competing financial interest.

**ACKNOWLEDGMENTS** 

We acknowledge funding from the Air Force Office of Scientific Research MURI program

(FA9550-16-1-0031 and FA9550-15-1-0514), the National Science Foundation (CMMI-1635443),

the Office of Naval Research (N00014-16-1-2333), and Kley Dom Biomimetics, LLC. This work

also used the Extreme Science and Engineering Discovery Environment, which is supported by

the National Science Foundation (ACI-1053575). IB acknowledges the support of the National

Institute of Biomedical Imaging and Bioengineering (2-P41-EB015871-31) and National Institute

of General Medical Sciences (DP2GM128198).

20

#### **REFERENCES**

(1) Labib, M.; Sargent, E. H.; Kelley, S. O. Chem. Rev. 2016, 116, 9001–9090.

- (2) Eleftheriadou, M.; Pyrgiotakis, G.; Demokritou, P. Curr. Opin. Biotechnol. 2017, 44, 87–93.
- (3) Zhou, Q.; Son, K.; Liu, Y.; Revzin, A. Annu. Rev. Biomed. Eng. 2015, 17, 165–190.
- (4) Weiz, S. M.; Medina-Sánchez, M.; Schmidt, O. G. Adv. Biosyst. 2017, 2, 1700193.
- (5) Gawad, C.; Koh, W.; Quake, S. R. Nat. Rev. Genet. 2016, 17, 175–188.
- (6) Vasdekis, A. E.; Stephanopoulos, G. Metab. Eng. 2015, 27, 115–135.
- (7) Ding, S.-Y.; Yi, J.; Li, J.-F.; Ren, B.; Wu, D.-Y.; Panneerselvam, R.; Tian, Z.-Q. *Nat. Rev. Mater.* **2016**, *1*, 16021.
- (8) Pandey, R.; Paidi, S. K.; Valdez, T. A.; Zhang, C.; Spegazzini, N.; Dasari, R. R.; Barman, I. *Acc. Chem. Res.* **2017**, *50*, 264–272.
- (9) Henry, A.-I.; Sharma, B.; Cardinal, M. F.; Kurouski, D.; Van Duyne, R. P. *Anal. Chem.* **2016**, 88, 6638–6647.
- (10) Laing, S.; Gracie, K.; Faulds, K. Chem. Soc. Rev. 2016, 45, 1901–1918.
- (11) Stiles, P. L.; Dieringer, J. A.; Shah, N. C.; Van Duyne, R. P. Annu. Rev. Anal. Chem. **2008**, 1, 601–626.
- (12) Ko, H.; Singamaneni, S.; Tsukruk, V. V. Small **2008**, *4*, 1576–1599.
- (13) Si, K. J.; Guo, P.; Shi, Q.; Cheng, W. Anal. Chem. 2015, 87, 5263–5269.
- (14) Polavarapu, L.; Liz-Marzán, L. M. Phys. Chem. Chem. Phys. 2013, 15, 5288–5300.
- (15) Jackman, J. A.; Rahim Ferhan, A.; Cho, N.-J. Chem. Soc. Rev. 2017, 46, 3615–3660.
- (16) Kuku, G.; Altunbek, M.; Culha, M. Anal. Chem. 2017, 89, 11160–11166.
- (17) Malachowski, K.; Jamal, M.; Jin, Q.; Polat, B.; Morris, C. J.; Gracias, D. H. *Nano Lett.* **2014**, *14*, 4164–4170.
- (18) Li, M.; Kang, J. W.; Dasari, R. R.; Barman, I. Angew. Chem. Int. Ed. 2014, 53, 14115–14119.
- (19) Jin, Q.; Li, M.; Polat, B.; Paidi, S. K.; Dai, A.; Zhang, A.; Pagaduan, J. V.; Barman, I.; Gracias, D. H. *Angew. Chem. Int. Ed.* **2017**, *56*, 3822–3826.
- (20) Huang, N.-T.; Zhang, H.-L.; Chung, M.-T.; Seo, J. H.; Kurabayashi, K. *Lab Chip* **2014**, *14*, 1230–1245.
- (21) Kim, T.-H.; Lee, D.; Choi, J.-W. Live Cell. Biosens. Bioelectron. 2017, 94, 485–499.
- (22) Xu, W.; Ling, X.; Xiao, J.; Dresselhaus, M. S.; Kong, J.; Xu, H.; Liu, Z.; Zhang, J. *Proc. Natl. Acad. Sci. U. S. A.* **2012**, *109*, 9281–9286.
- (23) Ling, X.; Xie, L.; Fang, Y.; Xu, H.; Zhang, H.; Kong, J.; Dresselhaus, M. S.; Zhang, J.; Liu, Z. *Nano Lett.* **2010**, *10*, 553–561.
- (24) Huang, S.; Pandey, R.; Barman, I.; Kong, J.; Dresselhaus, M. ACS Photonics 2018, 5, 2978-2982.
- (25) Ling, X.; Huang, S.; Deng, S.; Mao, N.; Kong, J.; Dresselhaus, M. S.; Zhang, J. Acc. Chem. Res. **2015**, 48, 1862-1870.
- (26) Huang, S.; Ling, X.; Liang, L.; Song, Y.; Fang, W.; Zhang, J.; Kong, J.; Meunier, V.; Dresselhaus, M. S. *Nano lett.* **2015**, *15*, 2892-2901.
- (27) Yin, P. T.; Shah, S.; Chhowalla, M.; Lee, K.-B. Chem. Rev. 2015, 115, 2483–2531.
- (28) Blees, M. K.; Barnard, A. W.; Rose, P. A.; Roberts, S. P.; McGill, K. L.; Huang, P. Y.; Ruyack, A. R.; Kevek, J. W.; Kobrin, B.; Muller, D. A.; et al. *Nature* **2015**, *524*, 204–207.
- (29) Xu, W.; Kwok, K. S.; Gracias, D. H. Acc. Chem. Res. 2018, 51, 436-444.
- (30) Zhang, N.; Tong, L.; Zhang, J. Chem. Mater. **2016**, 28, 6426–6435.
- (31) Leem, J.; Wang, M. C.; Kang, P.; Nam, S. Nano Lett. 2015, 15, 7684–7690.
- (32) Xu, W.; Qin, Z.; Chen, C.-T.; Kwag, H. R.; Ma, Q.; Sarkar, A.; Buehler, M. J.; Gracias, D. H. Sci. Adv. **2017**, *3*, e1701084.
- (33) Wang, Y.; Zheng, Y.; Huang, C. Z.; Xia, Y. J. Am. Chem. Soc. 2013, 135, 1941–1951.
- (34) Camargo, P. H.; Au, L.; Rycenga, M.; Li, W.; Xia, Y. Chem. Phys. Lett. 2010, 484, 304-308.

- (35) Gu, X. W.; Ye, X.; Koshy, D. M.; Vachhani, S.; Hosemann, P.; Alivisatos, A. P. *Proc. Natl. Acad. Sci. U.S.A.* **2017**, *114*, 2836-2841.
- (36) Chen, Y.; Guo, F.; Jachak, A.; Kim, S. P.; Datta, D.; Liu, J.; Kulaots, I.; Vaslet, C.; Jang, H. D.; Huang, J.; Kane, A.; Shenoy, V. B.; Hurt, R. H. *Nano Lett.* **2012**, *12*, 1996–2002.
- (37) Patra, N.; Wang, B.; Král, P. Nano Lett. 2009, 9, 3766-3771.
- (38) Paulsen, J. D. **2018**, arXiv preprint arXiv:1804.07425.
- (39) Gu, C. D.; Xu X. J.; Tu, J. P. J. Phys. Chem. C 2010, 114, 13614-13619
- (40) Qin, Z.; Taylor, M.; Hwang, M.; Bertoldi, K.; Buehler, M. J. Nano Lett. 2014, 14, 6520-6525.
- (41) Min, K.; Aluru, N. R. Appl. Phys. Lett. 2011, 98, 013113.
- (42) Verrier, S.; Notingher, I.; Polak, J. M.; Hench, L. L. Biopolymers 2004, 74, 157–162.
- (43) Veloso, A. B.; Longo, J. P. F.; Muehlmann, L. A.; Tollstadius, B. F.; Souza, P. E. N.; Azevedo, R. B.; Morais, P. C.; da Silva, S. W. *Sci. Rep.* **2017**, *7*, 7175.
- (44) Hodges, M. D.; Kelly, J. G.; Bentley, A. J.; Fogarty, S.; Patel, I. I.; Martin, F. L.; Fullwood, N. J. ACS *Nano* **2011**, *5*, 9535-9541.
- (45) Cools, J.; Jin, Q.; Yoon, E.; Alba Burbano, D.; Luo, Z.; Cuypers, D.; Callewaert, G.; Braeken, D.; Gracias, D. H. *Adv. Sci.* **2018**, *5*, 1700731.

# Self-folding hybrid graphene skin for 3D biosensing

Weinan Xu,<sup>†</sup> Santosh K. Paidi,<sup>‡</sup> Zhao Qin,<sup>§</sup> Qi Huang,<sup>†</sup> Chi-Hua Yu,<sup>§</sup> Jayson V. Pagaduan,<sup>†</sup> Markus J. Buehler,<sup>§</sup> Ishan Barman,<sup>‡</sup> David H. Gracias<sup>\*,†, $\nabla$ </sup>

#### **Table of Contents**

1. Materials and Methods	2
2. Raman characteristics of the G-NIPAM-G-Ag skin	5
3. Mechanical properties of the G-PNIPM-G-Ag skin	Ģ
4. Versatility of the hybrid graphene skin in terms of shape and composition	12
5. FEM simulation of the surface tension induced deformation	13
6. Estimation of the strain of the hybrid graphene skin on the pollen spike	15
7. Cell viability after wrapping with the G-PNIPAM-G-Ag skin	17
8. Raman spatial mapping of an unwrapped cancer cell	18
9. References	19

<sup>&</sup>lt;sup>†</sup>Department of Chemical and Biomolecular Engineering, Johns Hopkins University, Baltimore, Maryland 21218, USA

<sup>&</sup>lt;sup>‡</sup> Department of Mechanical Engineering, Johns Hopkins University, Baltimore, Maryland 21218, USA

<sup>§</sup> Department of Civil and Environmental Engineering, Massachusetts Institute of Technology, Cambridge, Massachusetts 02139, USA.

<sup>□</sup> Department of Oncology, The Johns Hopkins University School of Medicine, Baltimore, Maryland, 21287, USA

<sup>&</sup>lt;sup>⊥</sup> The Russell H. Morgan Department of Radiology and Radiological Science, The Johns Hopkins University School of Medicine, Baltimore, Maryland 21287, USA

 $<sup>^{\</sup>triangledown}$  Department of Materials Science and Engineering, Johns Hopkins University, Baltimore, Maryland 21218, USA

#### 1. Materials and Methods

#### 1.1. G-PNIPAM-G-Ag SERS substrate fabrication

Monolayer chemical vapor deposition (CVD) graphene (Graphene Supermarket, MA, USA) was transferred onto a silicon wafer using the PMMA method, and after dissolving the PMMA, it was immersed in a dilute aqueous solution of dopamine (2.0 mg/mL) (Sigma-Aldrich), buffered to a typical marine environment pH of 8.5 (10 mM tris-HCl), for 2 hours. A thin layer of polydopamine formed on the graphene surface via dopamine self-polymerization. The sample was washed thoroughly with deionized water and dried with N<sub>2</sub> gas. The polydopamine coated graphene was then immersed into a solution of amine-terminated PNIPAM (2.0 mg/mL) (Sigma-Aldrich, M<sub>n</sub>: 5,500) dissolved in 10 mM tris-HCl buffer (pH 8.5). The grafting reaction took place at 60 °C for 3h, and then cooled down to room temperature and further kept for 18 h. The functionalized graphene was thoroughly washed with deionized water and dried with N<sub>2</sub> gas.

After surface functionalization of graphene, another layer of CVD graphene was transferred on top as previously done using the PMMA method. Then the sample was immersed in an aqueous solution of Ag nanocubes (Ag NCs). The Ag NCs were synthesized via a polyol method as described earlier,<sup>1</sup> and the polyvinylpyrrolidone (PVP) ligands on the nanocube surface were replaced with cysteamine,<sup>2</sup> which facilitates strong bonding of the Ag NCs to the surface of graphene. After 3 hours of nanoparticle adsorption, the sample was taken out and rinsed thoroughly with deionized (DI) water and dried with N<sub>2</sub> gas. Rhodamine 6G (R6G) (Sigma-Aldrich) was dissolve in DI water to prepare its solution with different concentration, then the SERS substrate was immersed in the R6G solution for 2 h, and then washed thoroughly with DI water to remove unadsorbed molecules, and subsequently dried with N<sub>2</sub> gas.

# 1.2. Patterning of the G-PNIPAM-G-Ag skin and self-folding

To enable the selective binding of the hybrid graphene SERS structures to the substrate via van der Waals forces, a patterned aluminum (Al) sacrificial layer (40 nm) was deposited on top of a silicon wafer using lift-off metallization. As a result, there is no Al in the center part of each dumbbell shape, and everywhere else is cover with Al. Therefore, the center part of each dumbbell is in direct contact with the silicon wafer, the strong van der Waals force between silicon wafer

and ultrathin hybrid graphene can pin the center of the dumbbell to the substrate, while allowing folding of other parts with temperature increase.

The graphene was transferred onto such an Al patterned sacrificial layer on a silicon wafer and surface functionalized as described above. Then, a second layer of graphene was transferred on top. Before depositing the Ag NCs on the surface, the functionalized graphene was patterned into various shapes, including flower, dumbbell, and cruciform, by photolithography, and the graphene in the unwanted areas was removed using an oxygen plasma (RF power: 60W, time: 30s) (PE-100, Plasma Etch Inc.). Then, Ag NCs were selectively deposited on the graphene area by covering the undesired areas with photoresist.

The G-PNIPAM-G-Ag 2D patterns were released from the substrate by dissolving the underlying Al layer with dilute NaOH (5 mM); the solution also contains 3 mM of sodium dodecyl sulfate (SDS) surfactant, in order to reduce the adhesion of the graphene to the underlying surface and to prevent the graphene from permanently sticking to itself. A previous study showed that the presence of surfactant does not measurably affect the mechanical and electrical properties of the graphene.<sup>3</sup> Folding of the G-PNIPAM-G-Ag microstructures were induced by increasing the temperature after dissolving the Al sacrificial layer. The solution was heated using a hot plate to 37°C, and the temperature was monitored during the entire process with a thermometer.

#### 1.3. Characterization of G-PNIPAM-G-Ag films and microstructures

UV-Vis spectra were recorded using PerkinElmer (Lambda 950) UV/VIS/NIR spectrometer. The optical microscopy images were taken in an aqueous condition using a Nikon AZ100 microscope equipped with a C-HGFI mercury lamp. Confocal microscope images were collected and analyzed on a Zeiss LSM 700 confocal microscope (Carl Zeiss). Scanning electron microscope (SEM) images were taken with a field emission microscope (FE-SEM, JEOL JSM-6700, Tokyo, Japan). Raman spectra were collected on a Horiba Jobin Yvon LabRAM HR800 Raman microscope (Edison, NJ) using 532 nm excitation line. Spectra for each sample were obtained by measuring the Raman scattering of at least five separate spots on each sample and averaged. Nanoindentation was performed with the iNano Nanoindenter (Nanomechanics, Inc.) with a Berkovich tip. The sample film was suspended on a copper mesh with well-defined grid bars (spacing between the bars is 37 μm) to eliminate the influence of the substrate during indentation.

#### 1.4. 3D Raman mapping

The 3D Raman imaging was carried out using a Horiba Jobin Yvon Xplora<sup>TM</sup> PLUS confocal Raman microscope equipped with a motorized sample stage. A 532 nm laser was used for sample excitation. The laser was focused to have a beam diameter of approximately 540 nm using a 60× water immersion objective lens of 1.20 NA (Olympus) to deliver a power of approximately 60 W at the sample. Three-dimensional Raman mapping was done using a step size of 1 μm in both lateral and axial directions and was accomplished using the LabSpec 6 (Horiba) software. A series of 2D Raman maps were obtained at the preset planes along the Z axis. Each pixel in the 2D map contains the corresponding full Raman spectrum at that location. All the spectra were processed using MATLAB for polynomial baseline correction, and subsequently 2D maps were generated based on the intensity of a specific Raman peak. The reconstructed 3D Raman map was obtained by importing the peak intensity values to the corresponding coordinates in the 3D space using the Paraview software.

# 1.5. Cell culture and wrapping cells with the G-PNIPAM-G-Ag skin

We used the breast cancer cell line MDA-MB-231 (ATCC, Manassas, VA, USA) in this work. Cells were grown in DMEM media supplemented with 10% fetal bovine serum (FBS) and 1% penicillin-streptomycin in a humidified incubator at 37 °C and 5% CO<sub>2</sub>. The live/dead assay was performed by incubating the cells with calcein AM and ethidium homodimer-1 (Thermo Fisher Scientific, Rochester, NY, USA) in PBS solution at 37 °C for 30 min. The cells were then examined under an optical microscope.

For the experiments involving wrapping with the G-PNIPAM-G-Ag skin, the cells were first trypsinized and suspended in fresh culture media. Then the cell suspension was added to a Petri dish containing 2D dumbbell patterns of the G-PNIPAM-G-Ag skin. The elevated temperature during cell culture (37 °C) induces the folding of the G-PNIPAM-G-Ag structures, which encapsulate the cells after a few hours of incubation. The immunofluorescence images were obtained with a confocal microscope, where the green fluorescent antibody (Alexa Fluor 488) and blue fluorescent DAPI stain were used against fibronectin and DNA, respectively.

#### 2. Raman characteristics of the G-NIPAM-G-Ag skin

#### 2.1. The effect of second graphene layer on the Raman enhancement

The bottom graphene layer is surface functionalized with PNIPAM brushes to introduce the temperature responsive self-folding property. The second or top layer of graphene is transferred on the top of the G-PNIPAM layers prior to the deposition of Ag NCs. The second layer of graphene has two main roles: first, it enables the direct contact and intimate interaction between graphene and the plasmonic nanoparticles. The cumulative SERS enhancement signal of graphene and Ag NCs is stronger than graphene or Ag NCs alone. Second, by separating the Ag NCs from the underlying thin polymer layer, the localized surface plasmon enhancement from the Ag NCs is directed mostly to the analyte molecules on the surface, rather than the underlying PNIPAM brushes.

To investigate the role of the second graphene layer, we measured the Raman spectra of identical concentrations of R6G molecules on the G-PNIPAM-G-Ag skin, and a control sample without the second graphene layer: G-PNIPAM-Ag. It can be seen from Figure S1 that the G-PNIPAM-G-Ag skin has stronger SERS enhancement to the R6G molecules, and the overall spectrum is also cleaner.

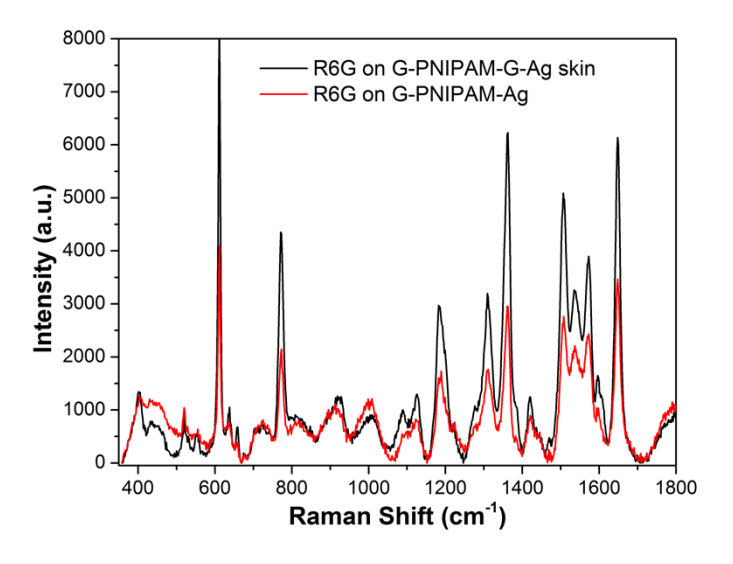


**Figure S1**. Raman spectra of Rhodamine 6G (10<sup>-3</sup> mol/L) on the G-PNIPAM-G-Ag skin as well as the G-PNIPAM-Ag substrate.

#### 2.2 The Raman enhancement factor of the G-PNIPM-G-Ag skin

The enhancement factor (EF) can be estimated as the ratio of Raman signal per molecule measured on the graphene SERS skin and the reference Raman signal per molecule originating from the sample in the normal Raman condition:

$$EF = \frac{I}{I_r} \times \frac{N_r}{N}$$

where I and  $I_r$  are the measured Raman intensity under SERS and normal Raman conditions; N and  $N_r$  are the number of sample molecules in the excitation volume under SERS and the normal Raman conditions, respectively. We used the strongest Raman band at 1646 cm<sup>-1</sup> to calculate the EF for R6G, the reference sample is bulk R6G crystal at normal Raman condition.

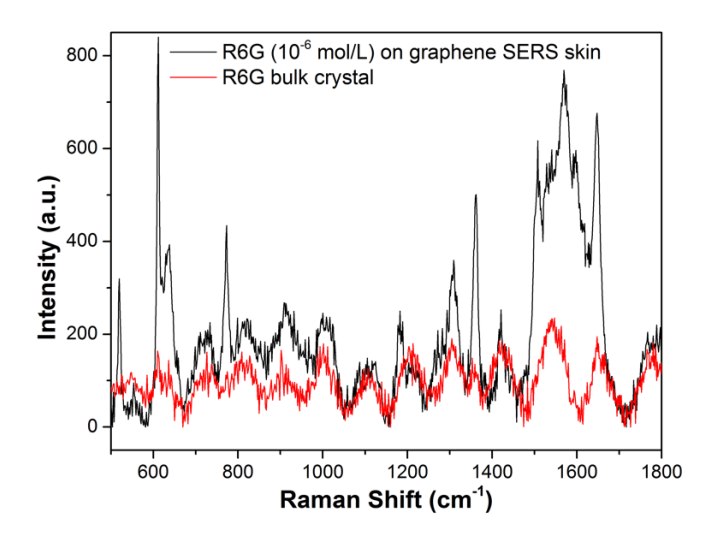


**Figure S2**. Raman spectra of Rhodamine 6G solid powder (a) and the SERS spectrum of R6G on the graphene SERS skin (b).

Taking the laser spot dimension (2.6  $\mu$ m in diameter), the penetration depth (~ 4.3  $\mu$ m), the density of R6G (0.79 g/cm³), we estimate  $N_r$  to be 2.27 x 10°. N can be estimated based on the total nanoparticles surface illuminated by the laser beam and the geometrical cross section of a individual R6G molecule, which is estimated to be 836 molecules.⁴ We measured the Raman peak intensity ratio  $\frac{I}{I_r}$  to be 3.9 (using the Raman spectrum of 10° mol/L R6G on graphene skin). Thus, we estimate the EF for R6G molecules on the graphene SERS skin to be 1.06 x 10°.

The EF for the cancer cell is more difficult to estimate, because the Raman signal from the control sample, which is the cancer cell on the quartz substrate is very weak at the same acquisition condition compared with the cell wrapped within the graphene SERS skin. From the peak intensity ratio, we estimate the EF for the lipid peak (1447 cm<sup>-1</sup>) from the cancer cell to be approximately 60, and the EF for protein peak (1002 cm<sup>-1</sup>) from the cancer cell to be approximately 110.

# 2.3. Comparison of the SERS enhancement with only graphene or Ag NCs

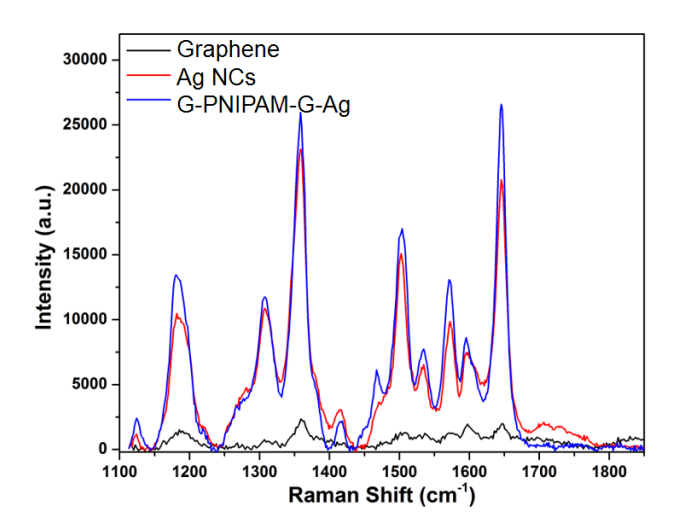


**Figure S3.** Raman spectra of R6G (50  $\mu$ M) on different substrates: pristine monolayer graphene (black), Ag NCs (red) and G-PNIPAM-G-Ag skin (blue). Although there is some intrinsic SERS enhancement by bare graphene, it is negligible compared to that obtained with the Ag NCs.

# 2.4. Raman signals from the components of the G-PNIPM-G-Ag skin

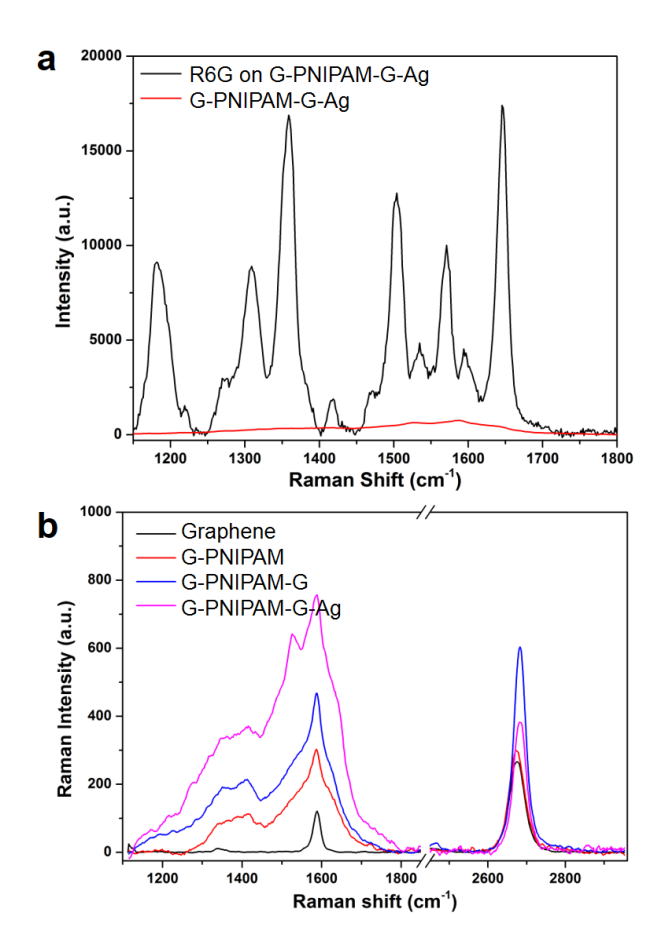


**Figure S4.** (a) Raman spectra from the G-PNIPAM-G-Ag skin itself and after deposition of R6G (5  $\mu$ M) on the skin. We observe that the background signal from the skin is negligible compared to that from the R6G. (b) Raman spectra of the G-PNIPAM-G-Ag skin (pink) and its components: pristine monolayer graphene (black), G-PNIPAM, (red), G-PNIPAM-G (blue). The Raman intensity scale is set to a low value in order to highlight the spectra. The result indicates that while the components show Raman features, their intensity is very low compared to R6G.

#### 3. Mechanical properties of the G-PNIPM-G-Ag skin

We performed nanoindentation tests to experimentally investigate the effect of the density of Ag NCs on the mechanical rigidity of the G-PNIPAM-G-Ag skin with different Ag NCs density. Briefly, the G-PNIPAM-G-Ag skin was fabricated on a copper mesh with well-defined grid bars (spacing between the bars is 37 µm), so that the film was suspended to eliminate the influence of the substrate during indentation. Nanoindentation was performed on the iNano Nanoindenter with a Berkovich tip. Representative indentation force vs displacement curves are shown in Figure S5 for the G-PNIPAM-G-Ag skin with three different Ag NC densities of 750, 1000 and 1800 per µm². It can be seen from the curves that the skin with the highest density of particles deflects the least or has the highest modulus and stiffness.

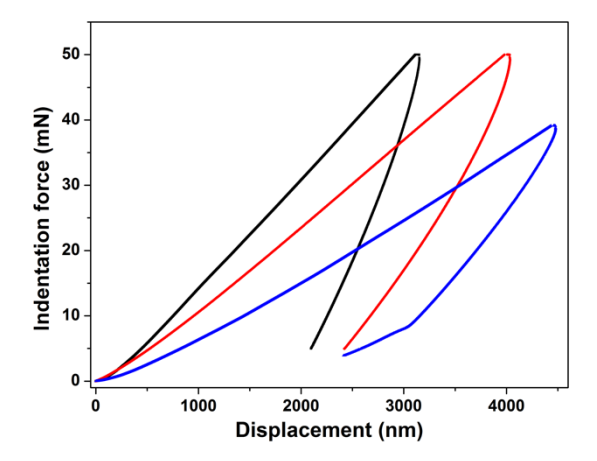


**Figure S5.** Representative force-displacement curves for the hybrid graphene skin with different Ag NCs density, obtained from nanoindentation tests.

The increase in stiffness with increasing density of Ag NCs can also be rationalized using a theoretical model. Assuming each Ag NP is cube-shaped, with an edge length l=20 nm, the nominal density of the Ag NC layer  $\rho$  can be calculated for the case when the Ag NC density is 1000 per  $\mu$ m<sup>2</sup> by,

$$\frac{\rho}{\rho_B} = \frac{NV\rho_{NC}}{l\rho_B} = 0.301$$

where bulk Ag density  $\rho_B$  is 10.5 g/cm<sup>3</sup>, the density of Ag NC,  $\rho_{NC}$  is 7.9 g/cm<sup>3</sup>, and N is 1000 per  $\mu$ m<sup>2</sup>, V is the volume of individual Ag NC.

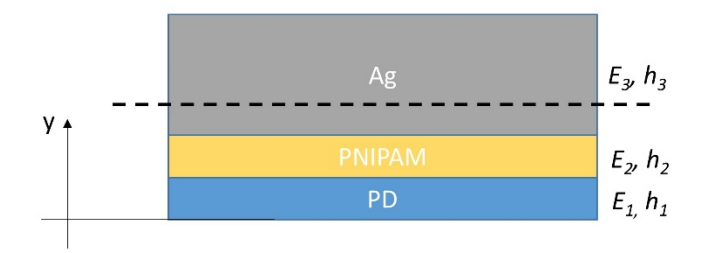
The Young's modulus E of a nanoporous metal can be estimated based on its relative density compared to that of the bulk metal, so  $E_3$  can be calculated by;<sup>6</sup>

$$\frac{E_3}{E_B} = 0.37 \left(\frac{\rho}{\rho_B}\right)^2 = 0.0335$$

where  $E_B = 83$  GPa for bulk silver. We can estimate that  $E_3 = 2.78$  GPa for the Ag NCs layer with a density N is 1000 per  $\mu$ m<sup>2</sup>.

The hybrid graphene skin can be regarded as a trilayer system, in which the bottom layer is polydopamine (PD), the middle layer is PNIPAM brushes, and the top is the Ag NCs layer. We can use thickness values for the three layers as 5, 5, and 20 nm, respectively. The Young's modulus of the PD and PNIPAM layers is 5GPa and 94 MPa according to our previous study.<sup>7</sup>

Based on this trilayer model, the distance from the outer surface of the hybrid graphene skin to its neutral axis (t) can be calculated by;



$$t = \frac{t_1 E_1 \cdot \frac{t_1}{2} + t_2 E_2 \cdot \left(t_1 + \frac{t_2}{2}\right) + t_3 E_3 \cdot \left(t_1 + t_2 + \frac{t_3}{2}\right)}{t_1 E_1 + t_2 E_2 + t_3 E_3} = 14.53 \text{ nm}$$

The bending stiffness D is given by

$$D = EI = \iint Ey^2 dA = E_1 \int_{-14.53}^{-9.53} y^2 dy + E_2 \int_{-9.53}^{-4.53} y^2 dy + E_3 \int_{-4.53}^{15.47} y^2 dy = 7211.2 \text{ nN} \cdot \text{nm}$$

where I is the second moment of inertia.

As a comparison, the bending stiffness of the functionalized graphene without the Ag NCs on the surface is:

$$D_0 = E_1 \int_{-2.59}^{2.41} y^2 dy + E_2 \int_{2.41}^{7.41} y^2 dy = 64.59 \text{ nN} \cdot \text{nm}$$

which is significantly smaller than that of the hybrid graphene skin.

Note that this calculation of the bending stiffness of the graphene skin is an extreme case, which assumes that the nanoparticle layer behaves like a continuous film, without any local displacement or rotation during bending. Alternatively, if the Ag NCs are free to rotate or move during bending, they will have a very small contribution to the bending stiffness; in this case, the bending stiffness would be very close to  $D_0$ . Therefore, the actual bending stiffness is in between the two extreme cases, and increases with the Ag NC density.

### 4. Versatility of the self-folding skin in terms of shape and composition

## 4.1. Self-folding of the hybrid graphene SERS skin with different shapes

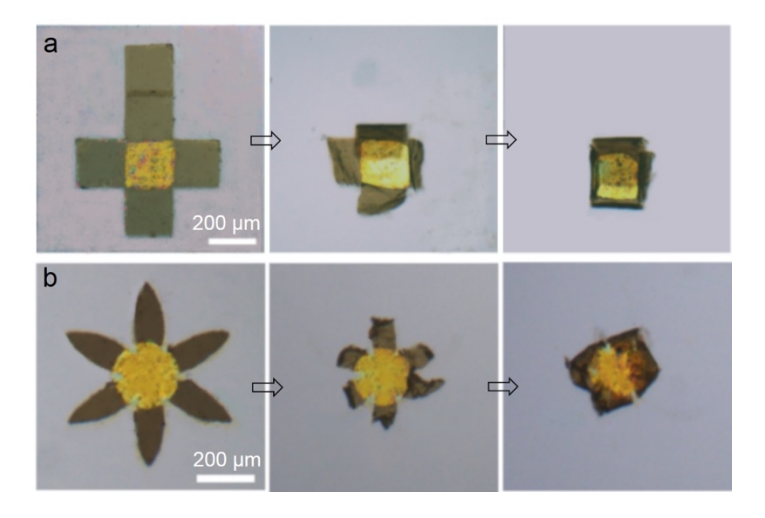


**Figure S6.** Optical microscopy snapshots of a, (a) box shaped, and (b) flower shaped G-PNIPAM-G-Ag skin in the flat state (left panel), during (center panel) and after (right panel) thermally triggered self-folding.

### 4.2. Self-folding of a hybrid graphene SERS skin with Au nanoparticles on surface

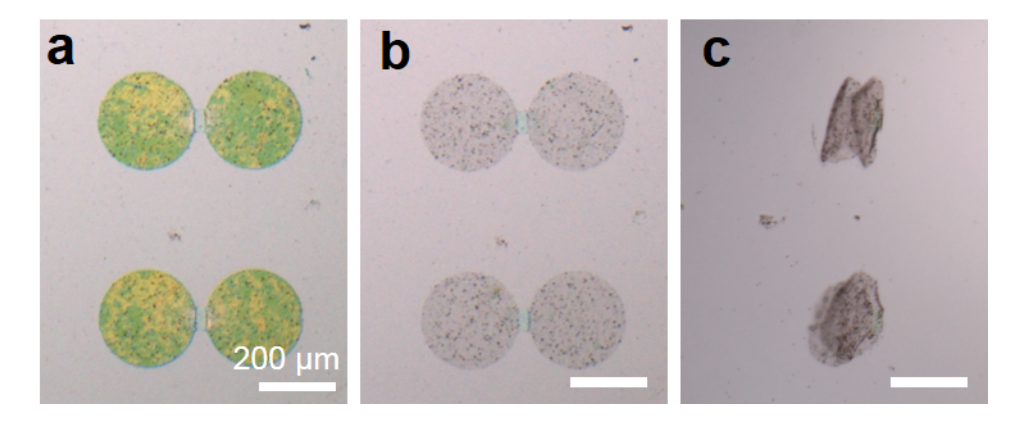


**Figure S7.** Optical microscopy snapshots of the self-folding of dumbbell patterned G-PNIPAM-G-Au SERS skin, and the gold nanoparticles are spherical with a diameter of 30 nm. Image of the G-PNIPAM-G-Au skin (a) after patterning into the dumbbell shape, (b) after dissolving the sacrificial layer, (c) after temperature induced self-folding. The result shows that it is feasible to use alternate plasmonic nanoparticles, with no significant change to the self-folding process.

#### 5. FEM simulation of the surface tension induced deformation

Considering that the bending stiffness of the hybrid graphene skin gets significantly larger after deposition of a high density Ag NCs on the surface, the internal strain mismatch from shrinkage of PNIPAM alone is not able to induce a fully collapsed configuration of the graphene skin, and the surface tension during water evaporation is important for the conformal encapsulation of a 3D object such as the silica microparticle shown in Figure 3.

To estimate the total Laplace pressure  $\sigma$  from surface tension, we assume that the entire folding process is slow and quasi-static and then can write the force balance condition as,

$$\pi R^2 \sigma = -2\pi R \gamma \cos \theta$$

where  $R=125~\mu m$  is the radius of the graphene skin,  $\gamma=72~mN/m$  is the surface tension of water and  $\theta$  is the contact angle between water and silver, which varies between 40° to 79° depending on the surface roughness.<sup>8</sup> We estimate  $\sigma$  between 219.8 (for  $\theta=79^{\circ}$ ) to 882.5 Pa (for  $\theta=40^{\circ}$ ), which is much larger than the self-weight of silver particles per unit area as 0.001 Pa, so its weight can be ignored.

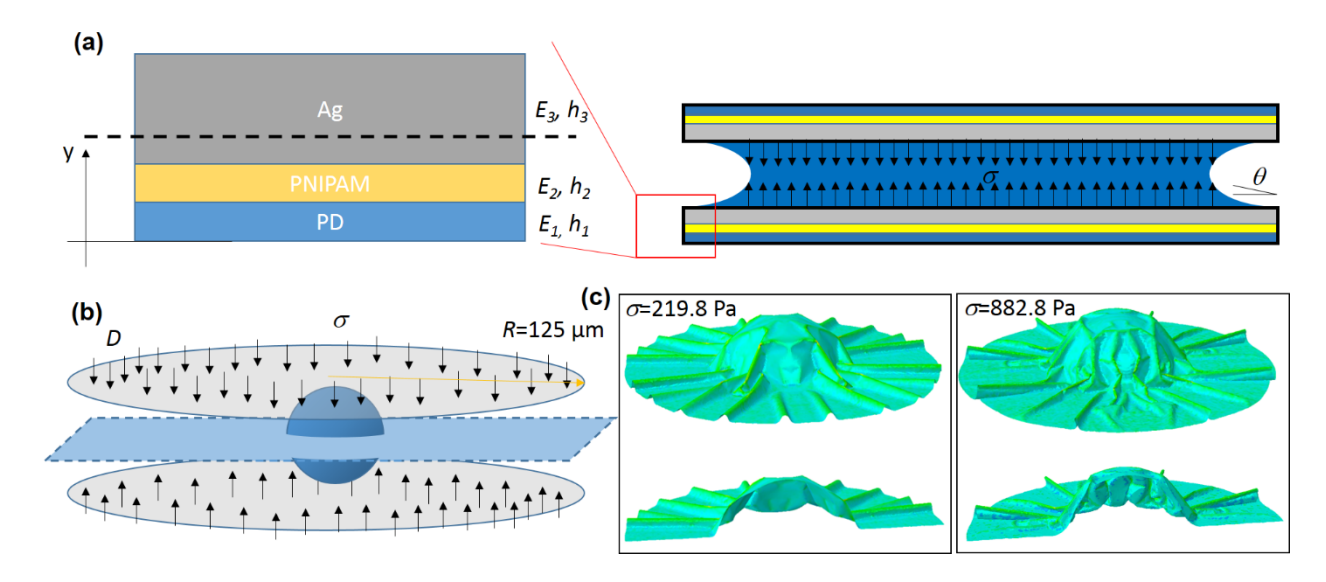


**Figure S8**. (a) Schematic of the cross-section of the hybrid graphene skin during the surface tension induced deformation. (b) Initial configuration of the system with a silica microparticle in between the hybrid graphene skin. (c) FEM results of the deformed graphene skin on the silica microparticle after full water evaporation, with Laplace pressure  $\sigma = 219.8$  Pa (left) and 882.8 Pa (right). Both the top view and section view of the shell model for the skin are shown, colored by principle in-plane strain within the neutral layer ( $\varepsilon = 0$  cyan,  $\varepsilon = 0.02$  green).

Using the material properties (t, D), geometric features (R, r) and loading conditions  $(\sigma)$ , we can build a finite element model (FEM) to compute the deformation of the graphene skin. The graphene skin is modeled as a thin shell with a bending stiffness of D and subject to Laplace pressure. The graphene skin after deformation will contact the top surface of the silica sphere with radius  $r=37.5 \mu m$ , which is modeled by a rigid sphere with a frictionless interface. By doing so, we can effectively simulate the evaporation of water from the gap between two graphene skin interfaces, generating the Laplace pressure to drive the complete closure of the skin.

The results, as shown in Figure S8, gives the deformation of one half of the hybrid graphene dumbbell, demonstrating that the pressure from water (for any  $\theta$  between 40° to 79°) is large enough to generate significant deformation to fully wrap up the silica microparticle. After wrapping, the strong van der Waals interaction between two membrane surfaces will stabilize the closed structure.

# 6. Estimation of the strain of the hybrid graphene skin on the pollen spike

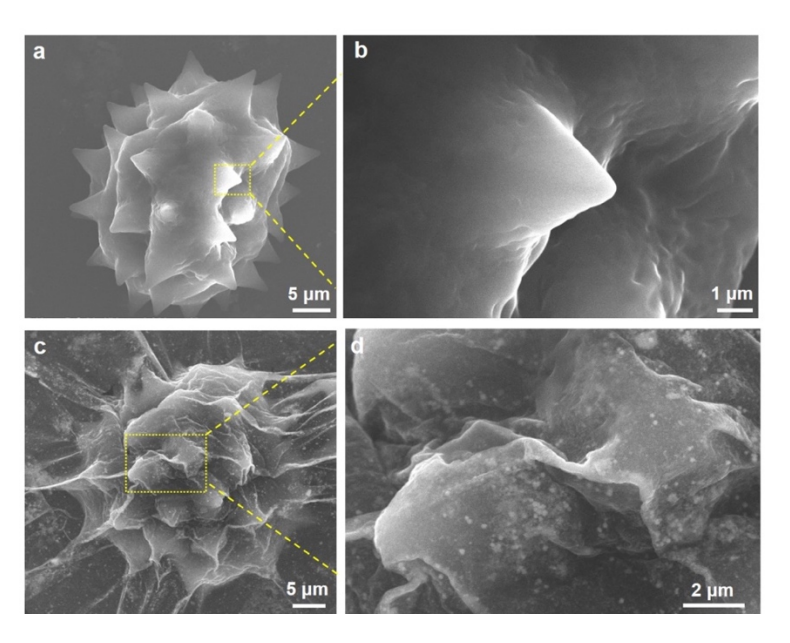
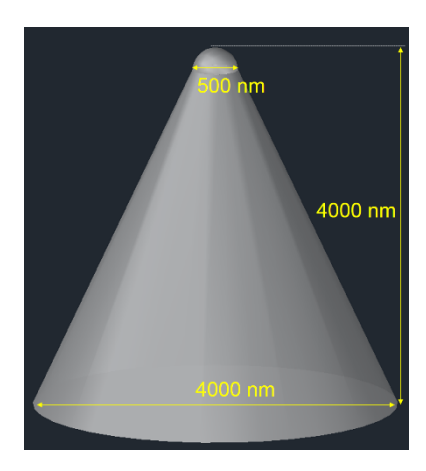


**Figure S9.** SEM images of a bare oxeye pollen grain (a-b) and a G-PNIPAM-G-Ag wrapped pollen grain (c-d) at different magnification. The G-PNIPAM-G-Ag skin conformally coats the surface of the grain including the spikes without observable fracture.

Based on the size measurement of the pollen spikes from SEM images above, the average geometry of the pollen spike is approximately equivalent to a cone with a rounded tip, as shown in Figure S9. The base diameter of the spike is  $4 \mu m$ , the total height is also  $4 \mu m$ , with a rounded tip with base length of 500 nm (as shown in scheme below).



Based on this approximation, the radius of a pristine pollen spike increases when moving from the bottom to the tip, with a maximum radius of 2000 nm at the bottom, and minimum of 275

nm at the tip. After conformal coating with the hybrid graphene SERS skin, the hybrid graphene has intimate contact with the pollen spike with some wrinkles on the surface. Therefore, if we assume perfect conformal contact, the radius of curvature of the graphene skin is approximately the same as the underlying pollen spike, with a maximum radius of curvature R = 275 nm at the tip.

The surface tensile strain is thereafter given by;

$$\varepsilon_{11} = \varepsilon_{22} = \frac{t}{2R}$$

where t is the distance from the outer surface of the graphene skin to its neutral axis, which is calculated to be 14.53 nm (see section 3 for details). Therefore, the biaxial strain of the graphene skin at the spike tip  $\varepsilon_{11} = \varepsilon_{22} = 0.026$ , which is well below the fracture strain of graphene, which is approximately 0.14 at room temperature.

#### 7. Cell viability after wrapping with the G-PNIPAM-G-Ag skin

The whole self-folding and wrapping process is done in aqueous condition, with the sample immersed in ample amount of water. In terms of the yield of wrapping of the target cell, cells are dropped onto the wafer and can fall on or off the patterned shape so in that sense the process is statistical and proportional to the area of coverage of the dumbbell. However, after falling on the dumbbell, the yield of encapsulation is very high (> 95%). This is because the size of breast cancer cells is in the range of 15-30  $\mu$ m, which is much smaller than the size of the two circles of the hybrid graphene dumbbell (250  $\mu$ m in diameter). Therefore, when seeded with a large enough number of cells during cell culture, we can guarantee that there are at least a few cells (usually >5) attached on the surface of each circle of the dumbbell. So when the hybrid graphene dumbbell fold toward the center, there are always several cells can be encapsulated inside.

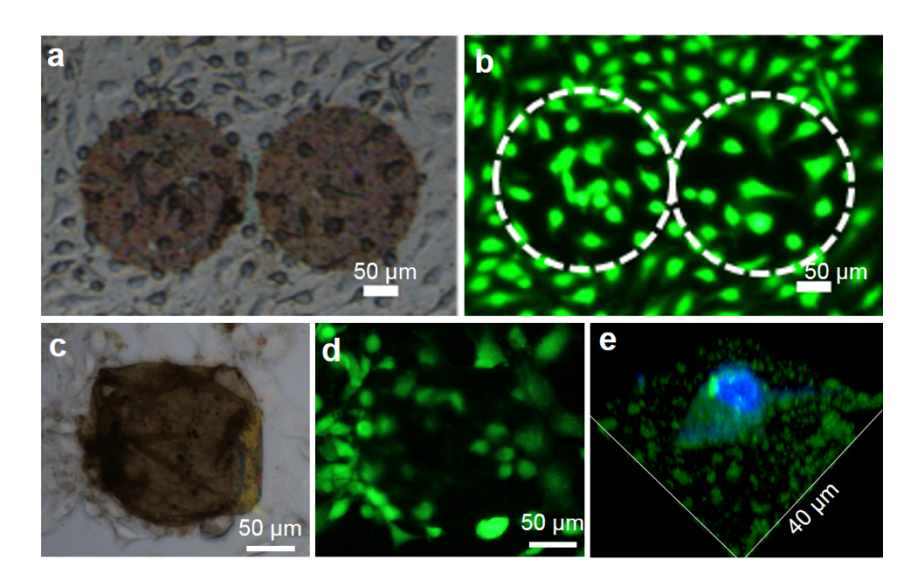


**Figure S10.** (a) Bright field optical and (b) fluorescence microscopy image of MDA-MB-231 cells cultured on the surface of a patterned G-PNIPAM-G-Ag dumbbell. The fluorescence images are obtained using a live/dead stain (calcein AM and ethidium homodimer-1) of the same sample, white circles correspond to the positions of G-Ag dumbbells. Green indicates live cells and red indicates dead cells. (c) Bright field and (d) fluorescence images of cells wrapped in the G-PNIPAM-G-Ag dumbbell after 48 hours. We observed that while the cells were wrapped there was adequate diffusion to permit viability for live cell biosensing applications. (e) 3D confocal immunofluorescence image of a single cell encapsulated within the G-PNIPAM-G-Ag skin, where the green fluorescent antibody (Alexa Fluor 488) and blue fluorescent DAPI stain were used against fibronectin and DNA, respectively.

# 8. Raman spatial mapping of an unwrapped cancer cell

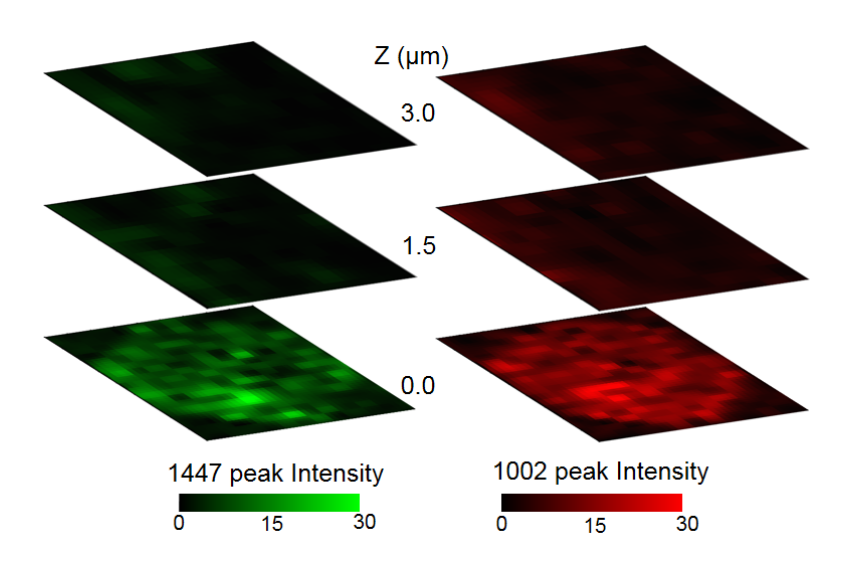


**Figure S11**. Raman mapping of the un-wrapped cancer cell on the G-PNIPAM-G-Ag skin at different focal planes along the Z axis, using the lipid peak at 1447 cm<sup>-1</sup> and protein peak at 1002 cm<sup>-1</sup>. As can be seen, for the unwrapped cell, SERS enhancement is seen only on the bottom of the cell in contact with the skin and the signal falls rapidly so that 3D spatial mapping is not possible.

#### References

\_

<sup>1</sup> Wang, Y.; Zheng, Y.; Huang, C. Z.; Xia, Y. J. Am. Chem. Soc. 2013, 135, 1941-1951.

<sup>2</sup> Moran, C. H.; Rycenga, M.; Zhang, Q.; Xia, Y. J. Phys. Chem. C 2011, 115, 21852-21857.

<sup>3</sup> Blees, M. K.; Barnard, A. W.; Rose, P. A.; Roberts, S. P.; McGill, K. L.; Huang, P. Y.; Ruyack, A. R.; Kevek, J. W.; Kobrin, B.; Muller, D. A.; et al. *Nature* **2015**, *524*, 204–207.

<sup>4</sup> Liu, D.; Wang, Q.; Hu, J. Appl. Surf. Sci. 2015, 356, 364-369.

<sup>5</sup> Tadjiki, S.; Montaño, M. D.; Assemi, S.; Barber, A.; Ranville, J.; Beckett, R. *Anal. Chem.* **2017**, *89*, 6056–6064.

<sup>6</sup> Huber, N.; Viswanath, R. N.; Mameka, N.; Markmann, J.; Weißmüller, J. *Acta Mater*. **2014**, *67*, 252-265. 7 Xu, W.; Qin, Z.; Chen, C.-T.; Kwag, H. R.; Ma, Q.; Sarkar, A.; Buehler, M. J.; Gracias, D. H. *Sci. Adv.* **2017**, *3*, e1701084.

<sup>8</sup> Gu, C. D.; Xu X. J.; Tu, J. P. J. Phys. Chem. C 2010, 114, 13614-13619

<sup>9</sup> Min, K.; Aluru, N. R. Appl. Phys. Lett. 2011, 98, 013113.